

# Toward background-free RENP using a photonic crystal waveguide

Minoru Tanaka<sup>1,\*</sup>, Koji Tsumura<sup>2</sup>, Noboru Sasao<sup>3</sup>, and Motohiko Yoshimura<sup>3</sup>

<sup>1</sup>*Department of Physics, Graduate School of Science, Osaka University, Osaka 560-0043, Japan*

<sup>2</sup>*Department of Physics, Kyoto University, Kyoto 606-8502, Japan*

<sup>3</sup>*Research Institute for Interdisciplinary Science, Okayama University, Okayama 700-8530, Japan*

\*E-mail: tanaka@phys.sci.osaka-u.ac.jp

Received January 11, 2017; Revised February 28, 2017; Accepted February 28, 2017; Published April 5, 2017

.....  
We study how to suppress multiphoton emission background in QED against radiative emission of a neutrino pair (RENP) from atoms. We pursue the possibility of background suppression using the photonic band structure of periodic dielectric media, called photonic crystals. The modification of photon emission rate in photonic crystal waveguides is quantitatively examined to clarify the condition of background-free RENP.  
.....

Subject Index     B54, C41, I85

## 1. Introduction

Radiative emission of a neutrino pair (RENP) is a novel process of atomic or molecular deexcitation in which a pair of neutrinos and a photon are emitted. It has been shown that the spectrum of the photon conveys information on unknown properties of the neutrinos, such as their absolute mass and the Majorana/Dirac distinction [1,2]. The rate of RENP is strongly suppressed as far as an incoherent ensemble of atoms is considered. In the proposed experiment [3], a rate enhancement mechanism with a macroscopic target of coherent atoms is employed. This macrocoherent enhancement mechanism, applicable to processes of plural particle emission, is experimentally shown to work as expected in a QED two-photon emission process [4,5], paired superradiance (PSR) [6].

In order to observe the RENP process and reveal the nature of neutrinos in an experiment, we have to understand the background processes. It has been shown that the three-photon emission process  $|e\rangle \rightarrow |g\rangle + \gamma + \gamma + \gamma$  is also amplified when the RENP  $|e\rangle \rightarrow |g\rangle + \gamma + \nu\bar{\nu}$  is macrocoherently enhanced [7]. The rate of the macrocoherent QED process of three-photon emission (McQ3) is found to be  $O(10^{20})$  Hz for the transition from the xenon  $|e\rangle = 6s^3P_1$  state of 8.437 eV excitation energy to the ground state  $|g\rangle = 5p^1S_0$ , while the RENP rate of the same transition is  $O(10^{-3})$  Hz. Therefore, though reducible, the McQ3 process is a serious background of the RENP process and the suppression of McQ3 (and similar  $n$ -photon emission processes, McQn) is mandatory.

An experimental scheme free of the McQn background is proposed to overcome this difficulty [7]. The essential idea is to suppress the emission of background photons in the McQn process using a waveguide, like cavity QED [8–11]. There exist cutoff frequencies  $\omega_c$  of the field eigenmodes in a waveguide (of a perfect conductor), which may be interpreted as the photon acquiring a mass of  $\hbar\omega_c$  in the waveguide. For instance, the smallest cutoff is  $\omega_c = \pi/b \simeq 0.6$  (1 mm/ $b$ ) meV for a square waveguide of size  $b$ . It has been proven that McQn is kinematically prohibited while RENP is

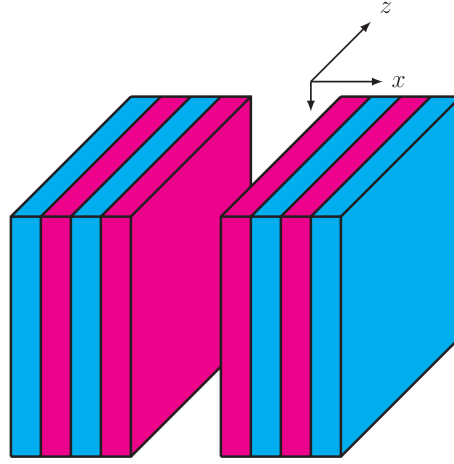


**Fig. 1.** Slab waveguide.

allowed in an appropriate region of trigger frequency if the smallest cutoff is larger than the neutrino mass, and thus background-free RENP is possible in principle.

The optical frequencies, however, are most relevant to the RENP signal triggered by lasers. Since even superconductors are far from a perfect conductor in the optical region, realization of the above idea is not straightforward. As a more realistic proposal, the use of photonic crystal is mentioned in Ref. [7]. A photonic crystal is an artificial periodic dielectric medium and exhibits a band structure in photon dispersion like the electronic band structure of a solid [12–14]. The emission of photons is forbidden in the band gap because of the null density of states. Hence, McQn is prohibited provided that at least one of the photons involved in the process falls in the band gap.

In this paper, we study the rate of McQn, especially McQ3, in photonic waveguides in order to clarify the possibility of suppression relative to RENP. We first describe the simplest photonic crystal waveguide, namely a slab waveguide [15], in Sect. 2. The band structure of a slab waveguide is shown and the Purcell factor [8], which quantifies the suppression or enhancement of emission in an environment, is introduced. In Sect. 3, we examine a photonic crystal waveguide of concentric stratified structure with a hollow core (Bragg fiber [16], in short) as a structure suitable for a RENP experiment. The rate of McQ3 in Bragg fiber is evaluated and the specification required for sufficient suppression of McQ3 is shown in Sect. 4. Section 5 is devoted to summary and outlook.

## 2. Slab waveguide

The suppression of photon emission is illustrated most simply by taking a nearly periodic system in one space dimension. We thus describe the principle of manipulation of photon emissions in photonic crystals taking a slab waveguide as an example. A slab waveguide [15] is a system of two confronted infinite-area slabs of stratified dielectric media as illustrated in Fig. 1. The electromagnetic field is supposed to be confined in the space between two slabs (the core) by Bragg reflection and propagate to the  $z$  direction in the core.

### 2.1. Transfer matrix of a slab

Each slab of the slab waveguide has a periodic structure of alternating refractive index  $n_i = \sqrt{\epsilon_i \mu_i}$  ( $i = 0, 1, 2$ ) as shown in Fig. 2, where  $i = 0$  represents the regions of no dielectric medium, and  $i = 1(2)$  corresponds to the layer of thickness  $a_{1(2)}$  made of the first (second) kind of medium. We

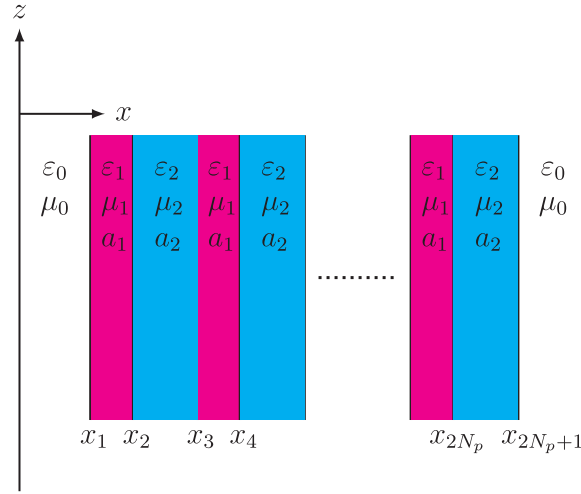


**Fig. 2.** Specification of the slab.

note that the permittivity  $\epsilon_i$  and the permeability  $\mu_i$  are relative ones, so that  $\epsilon_0 = \mu_0 = 1$ , and they are assumed real throughout this work. The positions of the slab surfaces and the layer interfaces are denoted by  $x_j$  ( $j = 1, 2, \dots, 2N_p + 1$ ), with  $N_p$  the number of layer pairs as indicated in Fig. 2.

A propagating field of angular frequency  $\omega$  and wave number  $\beta$  in the  $z$  direction is written as

$$\psi(t, x, y, z) = \psi(x)e^{i(\beta z - \omega t)}, \quad (1)$$

where  $\psi(x)$  satisfies the one-dimensional homogeneous Helmholtz equation

$$(\partial_x^2 + k_i^2)\psi(x) = 0, \quad k_i = \sqrt{\epsilon_i \mu_i \omega^2 - \beta^2}. \quad (2)$$

We assume translational symmetry in the  $y$  direction, hence  $y$  dependence is omitted. As in ordinary metal waveguides, the fields in the slab waveguide are classified into the transverse magnetic and electric (TM and TE) modes [17]. For the TM (TE) mode,  $\psi = E_z$  ( $H_z$ ) and other components of fields are derived from  $E_z$  ( $H_z$ ), where  $\mathbf{E}$  ( $\mathbf{H}$ ) is the electric (magnetic) field.

The fields in each region or layer are given as follows:

$$E_z(x) = A_0 e^{ik_0 x} + B_0 e^{-ik_0 x}, \quad H_z(x) = C_0 e^{ik_0 x} + D_0 e^{-ik_0 x}, \quad (3)$$

in the region of  $0 < x < x_1$ ;

$$E_z(x) = A_{2j-1} e^{ik_1 \xi} + B_{2j-1} e^{-ik_1 \xi}, \quad H_z(x) = C_{2j-1} e^{ik_1 \xi} + D_{2j-1} e^{-ik_1 \xi}, \quad (4)$$

for  $x_{2j-1} < x < x_{2j}$  ( $1 \leq j \leq N_p$ ) with the local coordinate  $\xi$  defined by  $x = x_{2j-1} + \xi$  ( $0 < \xi < a_1$ );

$$E_z(x) = A_{2j} e^{ik_2 \xi} + B_{2j} e^{-ik_2 \xi}, \quad H_z(x) = C_{2j} e^{ik_2 \xi} + D_{2j} e^{-ik_2 \xi}, \quad (5)$$

for  $x_{2j} < x < x_{2j+1}$  ( $1 \leq j \leq N_p$ ) with  $x = x_{2j} + \xi$  ( $0 < \xi < a_2$ );

$$E_z(x) = A_{2N_p+1} e^{ik_0 \xi} + B_{2N_p+1} e^{-ik_0 \xi}, \quad H_z(x) = C_{2N_p+1} e^{ik_0 \xi} + D_{2N_p+1} e^{-ik_0 \xi}, \quad (6)$$

for  $x_{2N_p+1} < x$  with  $x = x_{2N_p+1} + \xi$ . We note that the coefficients  $A$  ( $B$ ) and  $C$  ( $D$ ) represent the waves propagating toward the positive (negative)  $x$  direction.

The fields in adjacent regions satisfy the continuity conditions of  $E_z(x)$ ,  $H_z(x)$  and their derivatives at the boundary. Such conditions are conveniently described by using transfer matrices that relate the coefficients  $A$ ,  $B$ ,  $C$ , and  $D$  in different regions [18]. For the TM mode, we find the following connection formula:

$$\begin{pmatrix} A_{2N_p+1} \\ B_{2N_p+1} \end{pmatrix} = T_{\text{TM}} \begin{pmatrix} A_0 \\ B_0 \end{pmatrix}, \quad (7)$$

where the transfer matrix is defined by

$$T_{\text{TM}} := T_{\text{TM}}^{(e)} T_{\text{TM}}^{(1)} (T_{\text{TM}}^{(2)} T_{\text{TM}}^{(1)})^{N_p-1} T_{\text{TM}}^{(0)}, \quad (8)$$

with

$$T_{\text{TM}}^{(0)} = \frac{1}{2} \begin{pmatrix} (1 + \ell_{\text{TM}}^{(0)})e^{ik_0x_1} & (1 - \ell_{\text{TM}}^{(0)})e^{-ik_0x_1} \\ (1 - \ell_{\text{TM}}^{(0)})e^{ik_0x_1} & (1 + \ell_{\text{TM}}^{(0)})e^{-ik_0x_1} \end{pmatrix}, \quad \ell_{\text{TM}}^{(0)} = \frac{k_1 \varepsilon_0}{\varepsilon_1 k_0}, \quad (9)$$

$$T_{\text{TM}}^{(i)} = \frac{1}{2} \begin{pmatrix} (1 + \ell_{\text{TM}}^{(i)})e^{ik_i a_i} & (1 - \ell_{\text{TM}}^{(i)})e^{-ik_i a_i} \\ (1 - \ell_{\text{TM}}^{(i)})e^{ik_i a_i} & (1 + \ell_{\text{TM}}^{(i)})e^{-ik_i a_i} \end{pmatrix}, \quad i = 1, 2, \quad \ell_{\text{TM}}^{(1)} = \frac{k_2 \varepsilon_1}{\varepsilon_2 k_1} = \frac{1}{\ell_{\text{TM}}^{(2)}}, \quad (10)$$

and

$$T_{\text{TM}}^{(e)} = \frac{1}{2} \begin{pmatrix} (1 + \ell_{\text{TM}}^{(e)})e^{ik_2 a_2} & (1 - \ell_{\text{TM}}^{(e)})e^{-ik_2 a_2} \\ (1 - \ell_{\text{TM}}^{(e)})e^{ik_2 a_2} & (1 + \ell_{\text{TM}}^{(e)})e^{-ik_2 a_2} \end{pmatrix}, \quad \ell_{\text{TM}}^{(e)} = \frac{k_0 \varepsilon_2}{\varepsilon_0 k_2}. \quad (11)$$

As for the TE modes, we obtain

$$\begin{pmatrix} C_{2N_p+1} \\ D_{2N_p+1} \end{pmatrix} = T_{\text{TE}} \begin{pmatrix} C_0 \\ D_0 \end{pmatrix}, \quad (12)$$

where  $T_{\text{TE}}$  is given by exchanging  $\varepsilon_i$  and  $\mu_i$  in  $T_{\text{TM}}$ . We note that  $T_{\text{TM}}$  and  $T_{\text{TE}}$  are unimodular:  $\det T_{\text{TM}} = \det T_{\text{TE}} = 1$ . An elementary derivation of the transfer matrix is given in Appendix A.

## 2.2. Band structure of the slab

In the limit of a large number of layer pairs,  $N_p \rightarrow \infty$ , the surface effect can be neglected and the system has a strict periodicity of period  $a := a_1 + a_2$ . Then, the field obeys  $\psi(x + a) = e^{iKa} \psi(x)$ , as is well known as Bloch's theorem in quantum mechanics. In terms of the field coefficients (of odd layers), Bloch's theorem is expressed as

$$\begin{pmatrix} A_{2j+1} \\ B_{2j+1} \end{pmatrix} = e^{iK_{\text{TM}} a} \begin{pmatrix} A_{2j-1} \\ B_{2j-1} \end{pmatrix}, \quad \begin{pmatrix} C_{2j+1} \\ D_{2j+1} \end{pmatrix} = e^{iK_{\text{TE}} a} \begin{pmatrix} C_{2j-1} \\ D_{2j-1} \end{pmatrix}, \quad (13)$$

while, as described above,  $\psi(x)$  and  $\psi(x + a)$  are related by the transfer matrix of unit period,

$$\begin{pmatrix} A_{2j+1} \\ B_{2j+1} \end{pmatrix} = U_{\text{TM}} \begin{pmatrix} A_{2j-1} \\ B_{2j-1} \end{pmatrix}, \quad \begin{pmatrix} C_{2j+1} \\ D_{2j+1} \end{pmatrix} = U_{\text{TE}} \begin{pmatrix} C_{2j-1} \\ D_{2j-1} \end{pmatrix}, \quad (14)$$

where  $U_X := T_X^{(2)} T_X^{(1)}$  ( $X = \text{TM}, \text{TE}$ ) is unimodular.

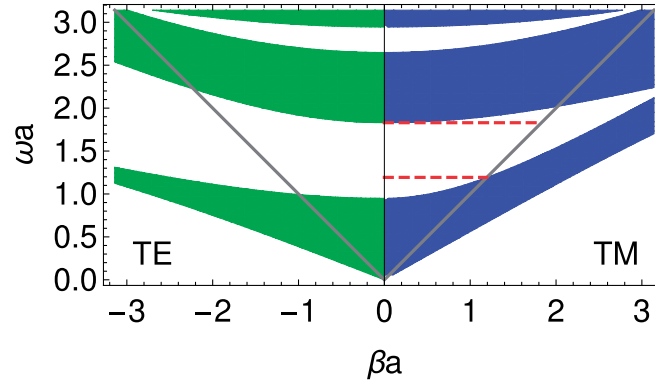


**Fig. 3.** Band structure of a dielectric slab. The parameters of the slab are  $n_1 = 4.6$ ,  $n_2 = 1.6$ , and  $\sqrt{n_1^2 - 1} a_1 = \sqrt{n_2^2 - 1} a_2$ . The blue (green) region is the allowed band of the TM (TE) mode.

It is obvious from Eqs. (13) and (14) that  $e^{iK_X a}$  is an eigenvalue of  $U_X$ , that is  $e^{iK_X a} = h^X \pm \sqrt{(h^X)^2 - 1}$ , where

$$h^X := \text{tr } U_X / 2 = \cos k_1 a_1 \cos k_2 a_2 - \frac{\ell_X^{(1)} + \ell_X^{(2)}}{2} \sin k_1 a_1 \sin k_2 a_2. \quad (15)$$

We see that  $h^X$  is real if  $k_1$  and  $k_2$  are real, which is the case above the light line, that is  $\omega \geq |\beta|$ , provided that  $n_{1,2} \geq 1$ . Then, the nature of the Bloch wave is determined by the magnitude of  $h^X$ : If  $(h^X)^2 < 1$ ,  $e^{iK_X a} = h^X \pm i\sqrt{1 - (h^X)^2}$  is a complex number of unit absolute value and thus  $K_X$  is real, namely the field is oscillating in the  $x$  direction. If  $(h^X)^2 > 1$ ,  $e^{iK_X a}$  is real and  $K_X$  is pure imaginary (modulo  $\pi/a$ ), namely the field is exponentially dumping (or growing) in the  $x$  direction. In other words, the region of  $(h^X)^2 < 1$  in the  $\beta$ – $\omega$  plane is the allowed band, and that of  $(h^X)^2 > 1$  is the forbidden band, forming the band gap. Therefore, the band edge is determined by the condition  $(h^X)^2 = 1$  [18].

In Fig. 3, we illustrate the band structure of a slab taking the example of dielectric media of  $n_1 = 4.6$  (tellurium-based glass) and  $n_2 = 1.6$  (polystyrene) [19]. The thicknesses of the layers are chosen to satisfy  $\sqrt{n_1^2 - 1} a_1 = \sqrt{n_2^2 - 1} a_2$ , which corresponds to the quarter-wave condition along the light line. The permeabilities are assumed to be  $\mu_{1,2} = 1$ . We present the allowed band of the TM (TE) mode for positive (negative)  $\beta$  as the blue (green) filled region. The diagonal solid lines show the light lines. We observe that the region of  $\omega$  between two red dashed lines is a complete band gap, namely no field exists in the slab for any  $|\beta| (< \omega)$  in this region of  $\omega$ . Thus, in the complete band gap, the Bragg reflection in the slab results in perfect reflection for any incident angle at the surface of the (semi-infinite) slab [20], and a pair of slabs placed face to face as shown in Fig. 1 would function as an optical waveguide.

It is useful in the following discussion of McQ3 suppression to understand how the first band gap is determined. For a quarter-wave stack, which satisfies  $k_1 a_1 = k_2 a_2 =: \phi$ , both the upper and lower boundaries of the first band gap are given by  $h_X = -1$ , namely

$$\cos \phi = \pm \sqrt{\frac{(\ell_X^{(1)} + \ell_X^{(2)})/2 - 1}{(\ell_X^{(1)} + \ell_X^{(2)})/2 + 1}}. \quad (16)$$

We note that  $\phi$  and  $\ell_X^{(1,2)}$  are functions of  $\beta$  and  $\omega$ , and thus Eq. (16) describes the boundary curves of the band gap in the  $\beta$ – $\omega$  plane.

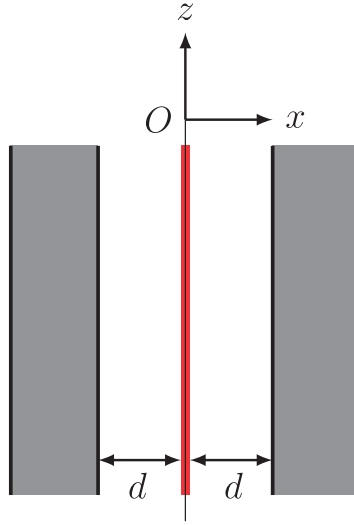


**Fig. 4.** Slab waveguide with a source (in solid red).

### 2.3. Emission in the slab waveguide

It is well known that the emission rate of photons in a cavity is modified from that in free space because of the change in the density of photon states [8–11]. Similarly, photonic crystals may be used to suppress optical emissions [12,13,21,22]. (For recent reviews, see e.g. Refs. [23,24].) The degree of suppression of an emission process is quantified by the ratio of the emission rate in an environment (a photonic crystal waveguide in the present work)  $\Gamma$  and that in free space  $\Gamma_{\text{FS}}$ ,  $F_P := \Gamma / \Gamma_{\text{FS}}$ , which is called the Purcell factor in the literature.

We consider the emission process from a localized source in the core of a slab waveguide as depicted in Fig. 4. The core size is  $2d$ , the source is uniform in the  $y$ - $z$  plane, and is placed at the center of the core. The slabs are of a finite number of layer pairs ( $N_p < \infty$ ) as in any realistic experiment, so that the prohibition in the band gap is not perfect, namely  $F_P \neq 0$ . Since the complete band gap is determined by the band gap of the TM mode as seen in Fig. 3, we evaluate the Purcell factor of the TM mode,  $\psi(x) = E_z(x)$ , in the following.

The field in the core in the presence of a source of unit strength is described by the inhomogeneous Helmholtz equation,

$$(\partial_x^2 + k_0^2)E_z(x) = -\delta(x), \quad (17)$$

where the origin of the  $x$  coordinate is chosen to be the position of the source. One finds that the field is continuous at the position of the source and its derivative has a discontinuity there:

$$E_z(+0) - E_z(-0) = 0, \quad \partial_x E_z(+0) - \partial_x E_z(-0) = -1. \quad (18)$$

The field in the region of  $0 < x < d$  is expressed as

$$E_z(x) = A_0 e^{ik_0 x} + B_0 e^{-ik_0 x}. \quad (19)$$

For  $-d < x < 0$ , the symmetry of the system under flipping of the  $x$  coordinate dictates

$$E_z(x) = A_0 e^{-ik_0 x} + B_0 e^{ik_0 x}, \quad (20)$$

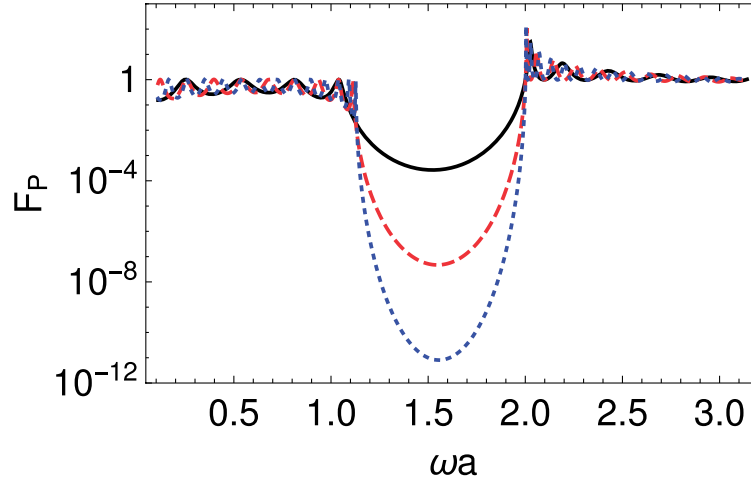


**Fig. 5.** Purcell factor near the light line,  $\beta a = \omega a - 0.1$ , in a slab waveguide of core size  $2d = 2.5a$ . Other parameters are the same as Fig. 3. The solid black, dashed red, and dotted blue lines represent  $N_p = 5, 10$ , and  $15$ , respectively.

so that the first equation in Eq. (18) is automatically satisfied. Substituting Eqs. (19) and (20) into the second equation of Eq. (18), we obtain

$$A_0 - B_0 = \frac{i}{2k_0}. \quad (21)$$

Since the emitter at  $x = 0$  is only the source, no incoming wave exists in the outside region of the slab waveguide. This defines the outgoing wave condition (known as the Sommerfeld radiation condition). In the region of  $x > x_{2N_p+1}$  in Fig. 2, this condition implies  $B_{2N_p+1} = 0$ . Then the connection formula in Eq. (7) leads to

$$\begin{pmatrix} A_{2N_p+1} \\ 0 \end{pmatrix} = T_{\text{TM}} \begin{pmatrix} A_0 \\ B_0 \end{pmatrix}. \quad (22)$$

The total outgoing flux is identified as

$$P = \frac{\omega \varepsilon_0}{k_0} |A_{2N_p+1}|^2. \quad (23)$$

It is straightforward to solve for  $A_{2N_p+1}$  from Eqs. (21) and (22):

$$A_{2N_p+1} = \frac{i}{2k_0} \frac{1}{(T_{\text{TM}})_{21} + (T_{\text{TM}})_{22}}, \quad (24)$$

where we have used the unimodularity of  $T_{\text{TM}}$ . The flux in the free space  $P_{\text{FS}}$  is given by putting  $T_{\text{TM}} = I$ , where  $I$  denotes the identity matrix. We thus find the expression of the Purcell factor in terms of the transfer matrix  $T_{\text{TM}}$  in Eq. (8),

$$F_P = \frac{P}{P_{\text{FS}}} = \frac{1}{|(T_{\text{TM}})_{21} + (T_{\text{TM}})_{22}|^2}. \quad (25)$$

In Fig. 5, we illustrate the Purcell factor of the slab waveguide whose parameters are specified by the core size  $2d = 2.5a$ , the refractive indices  $n_{1,2}$  and the layer thicknesses  $a_{1,2}$  being the same as Fig. 3, and the number of layer pairs  $N_p = 5$  (solid black),  $10$  (dashed red), and  $15$  (dotted blue).

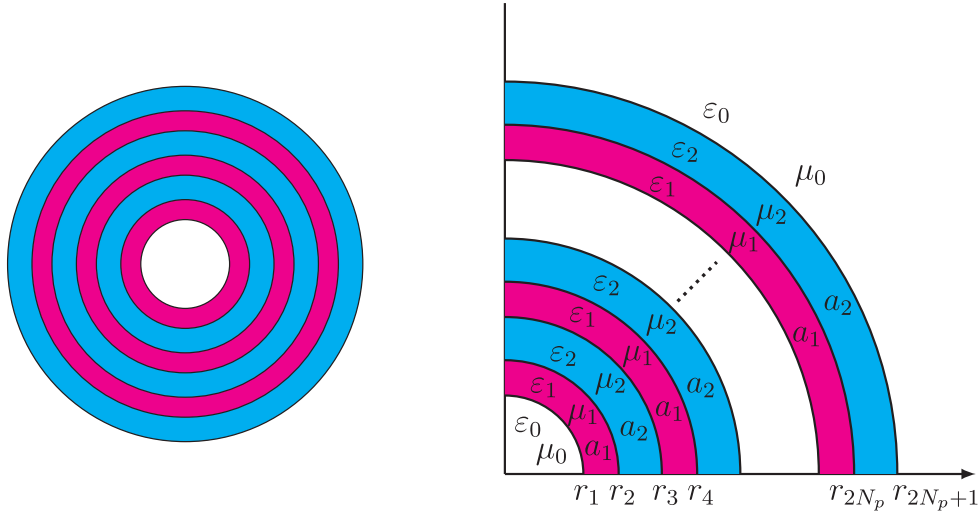


**Fig. 6.** Bragg fiber. Left: The whole cross section. Right: Specification of the Bragg fiber of alternating structure of layer pairs of thickness  $a_i$  ( $i = 1, 2$ ) with relative electric (magnetic) constant  $\epsilon_i$  ( $\mu_i$ ). The  $z$  direction is taken to be the fiber axis.

Given these parameters, the Purcell factor is a function of the frequency  $\omega$  and the wave number  $\beta$ . We choose the line  $\beta a = \omega a - 0.1$ , which is near the light line, motivated by the kinematics of McQ3 discussed in Sect. 4. The first band gap is clearly seen. Furthermore, we observe that the Purcell factor in the band gap decreases exponentially as  $N_p$  increases. This behavior is analytically confirmed for the large  $N_p$  limit in Appendix B.

### 3. Bragg fiber

Although the slab waveguide discussed above captures the essential idea of emission rate suppression in a photonic crystal waveguide, it is not realistic enough because of its unclosed core (in the  $y$  direction). In this section, we instead consider the Bragg fiber [16,25,26], which has a closed cross section as depicted in Fig. 6.

The fields propagating in the  $z$  direction are described in cylindrical coordinates as

$$\psi(t, r, \theta, z) = \psi(r, \theta) e^{i(\beta z - \omega t)}, \quad (26)$$

where  $\psi(r, \theta)$  satisfies the two-dimensional Helmholtz equation,  $(\nabla_t^2 + k_i^2)\psi(r, \theta) = 0$ . We take  $\psi = E_z$  and  $H_z$  independently so that the transverse ( $r$  and  $\theta$ ) components are given in terms of the derivatives of the  $z$  components.

#### 3.1. Transfer matrix of the Bragg fiber

The fields in the region of  $r_j < r < r_{j+1}$  are expressed as

$$E_z(r, \theta) = [A_j H_m^{(1)}(k_j r) + B_j H_m^{(2)}(k_j r)] e^{im\theta}, \quad (27)$$

$$H_z(r, \theta) = [C_j H_m^{(1)}(k_j r) + D_j H_m^{(2)}(k_j r)] e^{im\theta}, \quad (28)$$

where  $H_m^{(1,2)}$  are Hankel functions;  $A_j, B_j, C_j$ , and  $D_j$  are complex coefficients; and  $k_j = k_{1(2)}$  for odd (even)  $j$  in the range  $1 \leq j \leq 2N_p$ . The region of  $j = 0$ , that is  $0 = r_0 < r < r_1$ , is the hollow core, where the transverse wave number is given by  $k_0$ ; the region of  $r_{2N_p+1} < r$  ( $j = 2N_p + 1$ )



represents the exterior of the fiber, where  $k_{2N_p+1} = k_0$ . We note that the Hankel functions  $H_m^{(1)}$  and  $H_m^{(2)}$  represent the outgoing and incoming wave respectively.

The field coefficients  $\mathbf{v}_j := (A_j, B_j, C_j, D_j)^\top$  in the adjacent regions are related by the connection formula at the interface,

$$M_j(r_j)\mathbf{v}_j = M_{j-1}(r_j)\mathbf{v}_{j-1}, \quad (29)$$

where

$$M_j(r) = \begin{pmatrix} H_m^{(1)}(k_j r) & H_m^{(2)}(k_j r) & 0 & 0 \\ -\frac{\omega \varepsilon_j}{\beta k_j} H_m^{(1)'}(k_j r) & -\frac{\omega \varepsilon_j}{\beta k_j} H_m^{(2)'}(k_j r) & \frac{m}{k_j^2 r} H_m^{(1)}(k_j r) & \frac{m}{k_j^2 r} H_m^{(2)}(k_j r) \\ 0 & 0 & H_m^{(1)}(k_j r) & H_m^{(2)}(k_j r) \\ \frac{m}{k_j^2 r} H_m^{(1)}(k_j r) & \frac{m}{k_j^2 r} H_m^{(2)}(k_j r) & -\frac{\omega \mu_j}{\beta k_j} H_m^{(1)'}(k_j r) & -\frac{\omega \mu_j}{\beta k_j} H_m^{(2)'}(k_j r) \end{pmatrix}, \quad (30)$$

$\varepsilon_j = \varepsilon_{1(2)}$  for odd (even)  $j$  in the range  $1 \leq j \leq 2N_p$ ,  $\varepsilon_j = \varepsilon_0$  for  $j = 0, 2N_p + 1$ , and the same for  $\mu_j$ . The primed Hankel functions denote derivatives with respect to their own argument. Thus, the exterior coefficients are expressed in terms of the core coefficients using the transfer matrix  $T$ ,

$$\mathbf{v}_{2N_p+1} = T\mathbf{v}_0, \quad (31)$$

where

$$T := T_{2N_p+1} T_N \cdots T_2 T_1, \quad (32)$$

and

$$T_j := [M_j(r_j)]^{-1} M_{j-1}(r_j). \quad (33)$$

The explicit formula for  $T_j$  is given in Appendix C. We note that  $E_z$  and  $H_z$  have to be finite at  $r = 0$ , which implies  $A_0 = B_0$  and  $C_0 = D_0$ .

### 3.2. Band structure of the Bragg fiber

The cladding of the Bragg fiber is not strictly periodic even in the limit of  $N_p \rightarrow \infty$ . However, it can be regarded as periodic in the asymptotic region  $k_j r \gg 1$  since the curvature is negligible [27]. Thus the Bragg fiber is expected to exhibit a band structure for sufficiently large  $N_p$ .

One finds that  $M_j(r)$  in Eq. (30) becomes block diagonal and the TM and TE modes are separated in the asymptotic region as in the slab case. Moreover, it turns out, using the asymptotic forms of the Hankel functions,

$$H_m^{(1,2)}(kr) \simeq \sqrt{\frac{2}{\pi kr}} e^{\pm i[kr - (2m+1)\pi/4]}, \quad (34)$$

that the field coefficients follow Eq. (14) with  $U_X$  of the same diagonal elements as the slab regardless of the value of  $m$ , provided that an appropriate phase redefinition of the coefficients is made in order to absorb the difference between the local coordinate employed in the formulation of the slab and

the global one in the Bragg fiber. Since the band structure is solely determined by the trace of  $U_X$ , as discussed in Sect. 2.2, the Bragg fiber has an identical band structure to the slab.

### 3.3. Purcell factor of the Bragg fiber

The emission from a source  $s(r, \theta)$  (uniform in the  $z$  direction) in the Bragg fiber is described by the inhomogeneous two-dimensional Helmholtz equation,  $(\nabla_t^2 + k_i^2)\psi(r, \theta) = s(r, \theta)$ , where one may write  $\psi(r, \theta) = \psi(r)e^{im\theta}$  and  $s(r, \theta) = s(r)e^{im\theta}$ . We consider a localized source of unit strength at the center of the core ( $r = 0$ ), namely  $s(r, \theta) = -\delta(r)/(2\pi r)$ . This implies  $m = 0$ , and the transfer matrix becomes block diagonal,

$$T = \begin{pmatrix} T_{\text{TM}} & 0 \\ 0 & T_{\text{TE}} \end{pmatrix}, \quad (35)$$

as seen in Eq. (30). The TM and TE modes are separated as in the case of the slab waveguide.

The solution of the inhomogeneous Helmholtz equation is given by the Green's function with the boundary condition of the outgoing wave,  $G(r) = (i/4)H_0^{(1)}(k_0 r)$ . Applying this solution to the TM mode, from which the complete band gap is deduced, we obtain the core field,

$$E_z(r) = \left(A_0 + \frac{i}{4}\right)H_0^{(1)}(k_0 r) + A_0 H_0^{(2)}(k_0 r), \quad (36)$$

as well as the exterior field,

$$E_z(r) = A_{2N_p+1}H_0^{(1)}(k_0 r), \quad (37)$$

where  $A_0 = B_0$  and the outgoing wave condition  $B_{2N_p+1} = 0$  are used.

The flux at the exterior surface ( $r > r_{2N_p+1}$ ) is given by

$$P = \frac{2\omega\epsilon_0}{k_0^2} |A_{2N_p+1}|^2. \quad (38)$$

Solving the TM part of Eq. (31),

$$\begin{pmatrix} A_{2N_p+1} \\ 0 \end{pmatrix} = T_{\text{TM}} \begin{pmatrix} A_0 + \frac{i}{4} \\ A_0 \end{pmatrix}, \quad (39)$$

with the help of the unimodularity of  $T_{\text{TM}}$ , we obtain

$$A_{2N_p+1} = \frac{i}{4} \frac{1}{(T_{\text{TM}})_{21} + (T_{\text{TM}})_{22}}. \quad (40)$$

In the free space,  $T_{\text{TM}}$  is the unit matrix, hence  $A_{2N_p+1} = i/4$ . Finally, we obtain an expression for the Purcell factor of the Bragg fiber as

$$F_P = \frac{P}{P_{\text{FS}}} = \frac{1}{|(T_{\text{TM}})_{21} + (T_{\text{TM}})_{22}|^2}. \quad (41)$$

We note that this expression has the same form as the slab waveguide in Eq. (25), but the content of  $T_{\text{TM}}$  of the Bragg fiber is different from that of the slab in general.

We present an example of the numerical evaluation of the Purcell factor in the Bragg fiber in Fig. 7. The refractive indices  $n_{1,2}$  and the thicknesses of layers  $a_{1,2}$  are the same as those in Fig. 3, and the

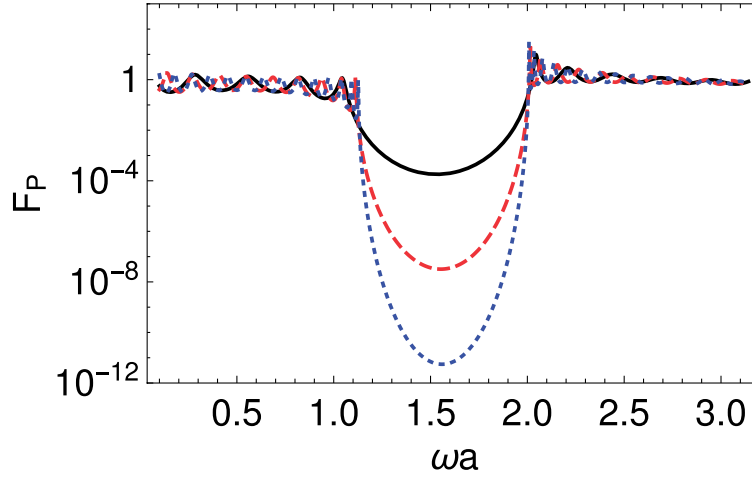


**Fig. 7.** Purcell factor of the Bragg fiber near the light line,  $\beta a = \omega a - 0.1$ . The core radius is  $r_1 = 2a$ , and other parameters are the same as in Figs. 3 and 5.

core radius is taken as  $r_1 = 2a$ . The solid black, dashed red, and dotted blue lines represent  $N_p = 5$ , 10, and 15, respectively. The position and the depth of the band gap is practically the same as the slab waveguide of the same layer structure and the Purcell factor in the band gaps exponentially decreases as the number of layer pairs increases, similarly to the slab waveguide. Hence, the McQn process in which at least one of the photons is emitted in the band gap can be strongly suppressed in the Bragg fiber.

#### 4. Suppression of McQ3 in the Bragg fiber

McQ3 has the largest rate among McQn's if it is allowed by the parity. In this section, we evaluate its rate in the Bragg fiber. We study a few combinations of refractive indices in order to clarify the necessary condition for sufficient background suppression compared to the RENP signal.

An experiment using a Xe gas target filling the core of a Bragg fiber is taken as an illustration. The Xe gas is prepared in a macrocoherent state [3] and the trigger laser irradiated along the fiber axis for the RENP process also induces the McQ3 background. As mentioned in Sect. 1, the deexcitation from  $|e\rangle = 6s^3P_1$  of 8.437 eV excitation energy to the ground state  $|g\rangle = 5p^1S_0$  is considered.

##### 4.1. McQ3 rate in free space

The free-space rate of the above Xe McQ3 process is explained in detail in Ref. [7]. To be self-contained, here we summarize the relevant formulae.

The differential spectral rate is given by

$$\frac{d\Gamma_{\text{FS}}}{d\omega_1} = \frac{\Gamma_0}{\omega_0} |D|^2 \omega_1^2 \omega_2^2, \quad (42)$$

where  $\Gamma_0$  is an overall rate, which is irrelevant here,  $\omega_0$  denotes the angular frequencies of the trigger light,  $\omega_{1,2}$  are those of emitted photons, the energy denominator  $D$  is written as

$$D(\omega_1) = \frac{1}{\omega_{pe} + \omega_0} \left( \frac{1}{\omega_{eg} - \omega_1} + \frac{1}{\omega_0 + \omega_1} \right) + \frac{1}{\omega_{pe} + \omega_1} \left( \frac{1}{\omega_{eg} - \omega_0} + \frac{1}{\omega_0 + \omega_1} \right) \\ + \frac{1}{\omega_{pg} - \omega_0 - \omega_1} \left( \frac{1}{\omega_{eg} - \omega_0} + \frac{1}{\omega_{eg} - \omega_1} \right), \quad (43)$$

and  $\hbar\omega_{eg} = 8.437$  eV is the excitation energy. We note that  $\omega_1$  and  $\omega_2$  are not independent once the trigger frequency is specified owing to energy conservation,  $\omega_{eg} = \omega_0 + \omega_1 + \omega_2$ . The spectral rate is obtained by integrating over  $\omega_1$ ,

$$\Gamma_{\text{FS}} = \int_{\omega_{eg}/2 - \omega_0}^{\omega_{eg}/2} d\omega_1 \frac{d\Gamma_{\text{FS}}}{d\omega_1}. \quad (44)$$

The magnitude of the longitudinal (with respect to the trigger) momentum of each emitted photon, which is necessary to evaluate the Purcell factor in the following, is dictated by the energy–momentum conservation satisfied in atomic processes with macrocoherence:

$$\beta_i = \omega_i |\cos \theta_i|, \quad i = 1, 2, \quad (45)$$

where

$$\cos \theta_i = \frac{\omega_{eg}}{\omega_0} - 1 - \frac{\omega_{eg}(\omega_{eg} - 2\omega_0)}{2\omega_0\omega_i}. \quad (46)$$

#### 4.2. McQ3 rate in the Bragg fiber

The rate of McQ3 is modified in the Bragg fiber and the modification is described by the Purcell factor discussed above. The differential rate in the Bragg fiber is represented as

$$\frac{d\Gamma_{\text{BF}}}{d\omega_1} = \frac{d\Gamma_{\text{FS}}}{d\omega_1} F_p(\omega_0, \beta_0) F_p(\omega_1, \beta_1) F_p(\omega_2, \beta_2), \quad (47)$$

where each Purcell factor is explicitly shown as a function of the corresponding photon's  $\omega$  and  $\beta$ . The Purcell factor for the trigger is omitted below because it is common for RENP (signal) and McQ3 (background).<sup>1</sup> Thus, the degree of background suppression by the Bragg fiber is given by

$$r_{\text{BF/FS}} = \frac{1}{\Gamma_{\text{FS}}} \int_{\omega_{eg}/2 - \omega_0}^{\omega_{eg}/2} d\omega_1 \frac{d\Gamma_{\text{FS}}}{d\omega_1} F_p(\omega_1, \beta_1) F_p(\omega_2, \beta_2). \quad (48)$$

In Fig. 8, we present the shape of the McQ3 differential rate in the Bragg fiber given in Eq. (47) for several combinations of refractive indices  $n_1$  and  $n_2$ . The structure of the Bragg fiber follows the quarter-wave stack condition along the light line, namely  $\sqrt{n_1^2 - 1} a_1 = \sqrt{n_2^2 - 1} a_2$ , as in Sect. 3.3, while the period  $a (= a_1 + a_2)$  is optimized to minimize  $r_{\text{BF/FS}}$ . We employ the number of layer pairs of  $N_p = 5$  as an illustration. The trigger frequency is chosen as  $\omega_0 = 0.95\omega_{eg}/2$  so that  $\omega_1 + \omega_2$  is slightly larger than  $\omega_{eg}/2$  as used in Ref. [7]. We note that the transverse length scale  $a$  of the Bragg fiber is of order  $1/\omega_{eg} \simeq 0.15 \mu\text{m}$ , which is much smaller than the scale of the metal waveguide in Sect. 1, and the supposed neutrino mass range below is  $\sim \omega_{eg}/4 \simeq 2$  eV or less.

We observe that the rate suppression is significant for relatively larger index differences,  $(n_1, n_2) = (4.6, 1.2)$ ,  $(4.8, 1.3)$ , and  $(5.0, 1.3)$ . In these cases, the band gap is wide enough such that at least one of the emitted photons is in the band gap owing to energy conservation. In the case of the combination  $(4.6, 1.6)$  employed in the fabrication of Bragg fiber in Ref. [19], however, the band gap is not

<sup>1</sup> It is evident that the density of neutrino states is hardly affected by the Bragg fiber (or photonic crystals in general). The trigger photon in RENP (and McQ3), however, is subject to the Purcell factor  $F_p(\omega_0, \beta_0)$ . Although the  $S/N$  ratio is independent of it, the absolute rate of RENP does depend on  $F_p(\omega_0, \beta_0)$ . It is required to choose the structure of the photonic crystal waveguide and the trigger parameters  $(\omega_0, \beta_0)$  such that  $F_p(\omega_0, \beta_0)$  is not strongly suppressed in the frequency range relevant to RENP.

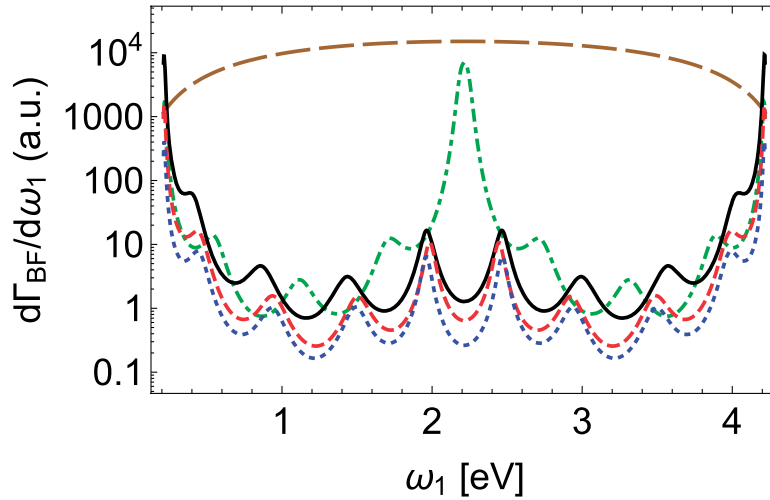


**Fig. 8.** The differential rate of McQ3 in the Bragg fiber of  $N_p = 5$  (in an arbitrary unit). The trigger frequency is  $\omega_0 = 0.95\omega_{eg}/2$ . The dot-dashed green, solid black, dashed red, and dotted blue lines show the cases of  $(n_1, n_2) = (4.6, 1.6)$ ,  $(4.6, 1.2)$ ,  $(4.8, 1.3)$ , and  $(5.0, 1.3)$  respectively. The free-space spectrum is also shown in the long-dashed brown line for comparison.

sufficiently wide and there is an energy range in which both of the photons are in the allowed band, as shown by the peak around  $\omega_1 \simeq 2.2$  eV.

In the case of infinite periodic structure described in Sect. 2.2, the boundaries of the band gap are determined by Eq. (16). Since the kinematics of McQ3 under present discussion requires  $\omega \sim \beta$ , the band gap near the light line is relevant. The crossing points of the light line and the boundaries of the first band gap are given by

$$\omega_{\pm a} = \frac{\sqrt{n_1^2 - 1} + \sqrt{n_2^2 - 1}}{\sqrt{n_1^2 - 1}\sqrt{n_2^2 - 1}} \arccos \left( \pm \sqrt{\frac{(\ell_{TM}^{(1)} + \ell_{TM}^{(2)})/2 - 1}{(\ell_{TM}^{(1)} + \ell_{TM}^{(2)})/2 + 1}} \right), \quad (49)$$

and

$$\frac{\ell_{TM}^{(1)} + \ell_{TM}^{(2)}}{2} = \frac{1}{2} \left( \frac{n_1^2 \sqrt{n_2^2 - 1}}{n_2^2 \sqrt{n_1^2 - 1}} + \frac{n_2^2 \sqrt{n_1^2 - 1}}{n_1^2 \sqrt{n_2^2 - 1}} \right). \quad (50)$$

We note that  $\omega_{+(-)}$  gives the lower (upper) boundary of the first band gap along the light line. We find that at least one of the emitted photons has an energy in the band gap and the McQ3 process is prohibited if  $2\omega_+ < \omega_-$ , provided that the period  $a$  is chosen to satisfy  $\omega_1 + \omega_2 = \omega_-$ . If the band gap is not wide enough such that this inequality is not satisfied, both photons are emitted in the first allowed band in part of the phase space and McQ3 is not prohibited. As seen in Fig. 8, this is the case for  $(n_1, n_2) = (4.6, 1.6)$ .

Figure 9 shows  $r_{BF/FS}$  as a function of  $N_p$ . Other parameters that define the structure of the Bragg fiber and the trigger frequency are the same as in Fig. 8. We find that, as expected, the dependence of  $r_{BF/FS}$  on  $N_p$  is approximately exponential for larger index differences. It turned out, on the other hand, that the rate suppression is not significant and practically independent of  $N_p$  for the combination of  $(4.6, 1.6)$ . This is due to the existence of the energy range in which both the photons are emitted in the allowed band as mentioned above.

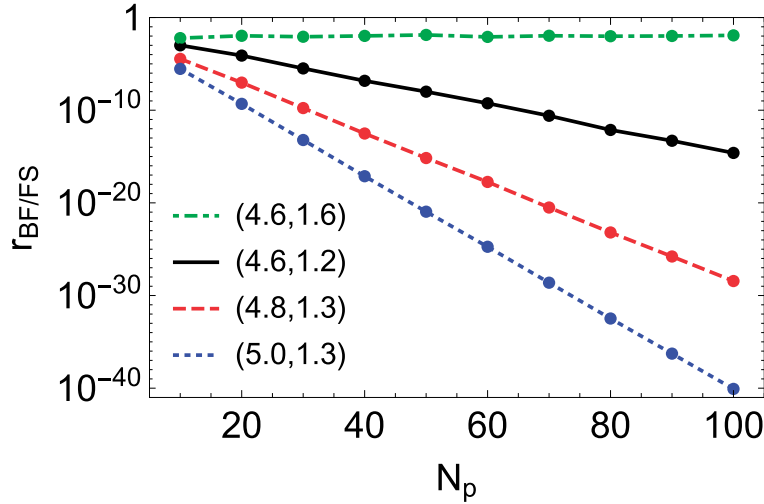


**Fig. 9.** McQ3 suppression factor in the Bragg fiber. The pairs of refractive indices  $(n_1, n_2)$  are chosen as indicated and the trigger frequency is  $\omega_0 = 0.95\omega_{eg}/2$ .

Hence the required suppression of McQ3 is attainable with Bragg fiber of finite  $N_p$  provided that a wide band gap is realized with a sufficiently large index difference and  $N_p$  is large enough.

## 5. Summary and outlook

We have studied the macrocoherently enhanced multiphoton process that is a potential source of serious background in the atomic neutrino process RENP. The proposal of background suppression using photonic crystals is examined in detail. The essential idea is the prohibition of photon emission in the band gap of photonic crystals.

Employing the method of a transfer matrix, the periodic dielectric structure of slab layers that has alternating refractive indices is shown to exhibit such a band structure because of the Bragg reflection at the interfaces of two dielectric media. The suppression of emission in the slab waveguide made of two finite slabs is quantified by the Purcell factor. We find that the Purcell factor decreases exponentially as the number of layer pairs  $N_p$  increases.

Then, as a more realistic experimental setup, the McQ3 process in the Bragg fiber is discussed. The Bragg fiber possesses a practically identical band structure and Purcell factor to the slab waveguide. The degree of McQ3 background suppression is given by  $r_{\text{BF/FS}}$  in Eq. (48), which compares the McQ3 rate in the Bragg fiber to that in free space. We have numerically evaluated  $r_{\text{BF/FS}}$  using the transfer matrix and found that it also decreases exponentially as  $N_p$  increases for sufficiently large index differences.

The Bragg fiber fabricated in the laboratory is made of dielectric media of  $n_1 = 4.6$  and  $n_2 = 1.6$  in the infrared region [19]. It was found that the suppression factor  $r_{\text{BF/FS}}$  does not scale exponentially for this pair of refractive indices because of the relatively narrower band gap. Our numerical results indicate that a larger index contrast such as (4.6, 1.2) is desirable for background rejection. Polymer of index  $\sim 1.3$  in the optical region is commercially available (e.g. CYTOP by AGC). To further reduce the index toward  $\sim 1.2$ , one may replace part of the material with a gas, like aerogels.

Even if synthesis of material of the required indices in the optical region is impossible, there are two possible ways to overcome the issue. One is to find a target or an experimental setup whose energy scale is low enough. Since the refractive index tends to be larger for lower frequencies, the

necessary index difference could be obtained with increased  $n_1$ . Another is to consider more elaborate structures than those discussed in the present work. For example, a set of slabs of periods  $a$  and  $2a$  may be combined. The lowest band gap of the latter locates at the upper half of the first allowed band of the former, so that their combination effectively exhibits a wider band gap. Both of these improvements are under investigation.

The higher-order macrocoherent QED processes McQn ( $n \geq 4$ ) are also potentially dangerous. In the case that McQ3 is allowed by the parity, the next allowed is McQ5 of five photons. As a concrete evaluation of the McQ5 rate is not available at present, we roughly estimate the ratio of McQ5 and McQ3 rates by counting the coupling and phase-space factors as  $\alpha^2/((4\pi)^4 2!3!) \sim O(10^{-10})$ , where  $\alpha$  is the fine structure constant. In addition to the native rate suppression, the photon veto is expected to be more effective for higher McQn. If a background photon emitted along the Bragg fiber is detected with 99.9% efficiency, the McQ5 rate is virtually reduced by  $(10^{-3})^4 = 10^{-12}$ . Combining the two suppression factors, McQ5 (or higher) seems rather harmless. (The photon veto is also helpful to mitigate the requirement for McQ3 suppression.)

To design a realistic RENP experiment, the method to excite the atoms/molecules in a macroscopic target to an appropriate state for neutrino emission should be studied in addition to the background processes. In the PSR experiments in Refs. [4,5], the initial coherent state of the macroscopic target is prepared by the Raman process with two parallel lasers propagating in the same direction. It turns out that a pair of counter-propagating lasers is necessary for the emission of massive neutrinos, unlike the PSR case in which the emitted particles are massless photons. A PSR experiment with a para-hydrogen target with counter-propagating lasers is in preparation at Okayama University in order to show that the macrocoherent emission of massive particles is possible.

In conclusion, the suppression mechanism of the McQ3 background in RENP by a photonic crystal waveguide works in principle. Other backgrounds of higher orders are relatively suppressed and the photon veto is effective for them. Further research and development work is necessary to design a background-free RENP experiment.

## Acknowledgements

This work is supported in part by JSPS KAKENHI Grant Numbers JP25400257 (MT), 15H02093 (MT, NS, and MY), 15K13468 (NS), and 16H00868 (KT).

## Appendix A. Derivation of the transfer matrix

The boundary condition of an electromagnetic field at an interface of two media is prescribed by Maxwell equations. The condition necessary to derive the transfer matrices is that the tangential components of  $\mathbf{E}$  and  $\mathbf{H}$  are continuous at the interface. Hence, in the case of the slab waveguide in Sect. 2, the tangential components of the fields satisfy the boundary conditions  $E_{y,z}(x_i - 0) = E_{y,z}(x_i + 0)$  and  $H_{y,z}(x_i - 0) = H_{y,z}(x_i + 0)$  at the interface of  $x = x_i$  ( $1 \leq i \leq 2N_p + 1$ ).

It also follows from Maxwell equations that the transverse (not tangential) components of the fields are given by derivatives of the longitudinal (i.e.  $z$ ) components, as mentioned in Sect. 2.1. For the slab waveguide, one finds

$$E_y(x) = -\frac{i}{k_i^2} \omega \mu_i \frac{\partial H_z}{\partial x}, \quad H_y(x) = \frac{i}{k_i^2} \omega \varepsilon_i \frac{\partial E_z}{\partial x}, \quad (\text{A1})$$

where  $i = 0, 1$ , or  $2$ . Thus the derivatives of  $E_z(x)$  and  $H_z(x)$  as well as  $E_z(x)$  and  $H_z(x)$  themselves are continuous at the interface.

Applying the above result to the interface at  $x = x_{2j}$  ( $1 \leq j \leq N_p$ ) of the slab waveguide, one obtains

$$A_{2j-1}e^{ik_1a_1} + B_{2j-1}e^{-ik_1a_1} = A_{2j} + B_{2j}, \quad (\text{A2})$$

from the continuity of  $E_z$ , and

$$\frac{\varepsilon_1}{k_1}(A_{2j-1}e^{ik_1a_1} - B_{2j-1}e^{-ik_1a_1}) = \frac{\varepsilon_2}{k_2}(A_{2j} - B_{2j}), \quad (\text{A3})$$

from the derivative of  $E_z$  (i.e.  $H_y$ ). A matrix representation of these equations gives the transfer matrix  $T_{\text{TM}}^{(1)}$  in Eq. (10). The other transfer matrices in the main text are obtained in the same manner.

## Appendix B. Large $N_p$ behavior of the Purcell factor

We use the Chebyshev identity,

$$U^n = \frac{1}{\lambda_+ - \lambda_-} \left[ (\lambda_+^n - \lambda_-^n)U - (\lambda_+^{n-1} - \lambda_-^{n-1})I \right], \quad (\text{B1})$$

where  $U$  is a unimodular two-by-two matrix whose eigenvalues are  $\lambda_{\pm}$ . Since  $U_{\text{TM}} := T_{\text{TM}}^{(2)}T_{\text{TM}}^{(1)}$  is unimodular, the transfer matrix in Eq. (8) is represented as

$$T_{\text{TM}} = \left( \lambda_+^{N_p-1} - \lambda_-^{N_p-1} \right) S_1 - \left( \lambda_+^{N_p-2} - \lambda_-^{N_p-2} \right) S_0, \quad (\text{B2})$$

where

$$S_j := \frac{1}{\lambda_+ - \lambda_-} T_{\text{TM}}^{(e)} T_{\text{TM}}^{(1)} U_{\text{TM}}^j T_{\text{TM}}^{(0)} \quad (j = 0, 1) \quad (\text{B3})$$

is independent of  $N_p$  and the eigenvalues  $\lambda_{\pm}$  of  $U_{\text{TM}}$  are given by

$$\lambda_{\pm} = h^{\text{TM}} \pm \sqrt{(h^{\text{TM}})^2 - 1}, \quad h^{\text{TM}} := \frac{1}{2} \text{tr } U_{\text{TM}}. \quad (\text{B4})$$

The elements of the transfer matrix  $T_{\text{TM}}$  are given by

$$(T_{\text{TM}})_{22} = \left( \lambda_+^{N_p-1} - \lambda_-^{N_p-1} \right) a_1 - \left( \lambda_+^{N_p-2} - \lambda_-^{N_p-2} \right) a_0, \quad (\text{B5})$$

$$(T_{\text{TM}})_{21} = \left( \lambda_+^{N_p-1} - \lambda_-^{N_p-1} \right) b_1 - \left( \lambda_+^{N_p-2} - \lambda_-^{N_p-2} \right) b_0, \quad (\text{B6})$$

where

$$S_j = \begin{pmatrix} a_j^* & b_j^* \\ b_j & a_j \end{pmatrix}. \quad (\text{B7})$$

The inequality  $(h^{\text{TM}})^2 > 1$  is satisfied in the band gap, as described in Sect. 2.2. For  $h^{\text{TM}} > 1$ , we find  $\lambda_+ > 1 > \lambda_- > 0$  and

$$(T_{\text{TM}})_{22} \simeq \lambda_+^{N_p-2} (\lambda_+ a_1 - a_0), \quad (\text{B8})$$

$$(T_{\text{TM}})_{21} \simeq \lambda_+^{N_p-2} (\lambda_+ b_1 - b_0), \quad (\text{B9})$$



as  $N_p \rightarrow \infty$ . For  $h^{\text{TM}} < -1$ ,  $\lambda_- < -1 < \lambda_+ < 0$  and

$$(T_{\text{TM}})_{22} \simeq -\lambda_-^{N_p-2} (\lambda_- a_1 - a_0), \quad (\text{B10})$$

$$(T_{\text{TM}})_{21} \simeq -\lambda_-^{N_p-2} (\lambda_- b_1 - b_0). \quad (\text{B11})$$

Thus we obtain

$$F_P \simeq \frac{|\lambda_{\pm}|^{-2(N_p-2)}}{|\lambda_{\pm}(a_1 + b_1) - (a_0 + b_0)|^2} \propto e^{-2N_p \log |\lambda_{\pm}|}, \quad h^{\text{TM}} \gtrless \pm 1, \quad (\text{B12})$$

for large  $N_p$ , i.e.  $F_P$  exponentially decreases as  $N_p$  increases.

### Appendix C. Explicit expression for $T_j$

We present the matrix elements of  $T_j$  defined in Eq. (33):

$$\begin{aligned} (T_j)_{11} &= (T_j)_{22}^* \\ &= i \frac{\pi}{4} k_j r_j \left[ H_m^{(1)}(k_{j-1} r_j) H_m^{(2)'}(k_j r_j) - \frac{\varepsilon_{j-1} k_j}{\varepsilon_j k_{j-1}} H_m^{(1)'}(k_{j-1} r_j) H_m^{(2)}(k_j r_j) \right], \end{aligned} \quad (\text{C1})$$

$$\begin{aligned} (T_j)_{12} &= (T_j)_{21}^* \\ &= i \frac{\pi}{4} k_j r_j \left[ H_m^{(2)}(k_{j-1} r_j) H_m^{(2)'}(k_j r_j) - \frac{\varepsilon_{j-1} k_j}{\varepsilon_j k_{j-1}} H_m^{(2)'}(k_{j-1} r_j) H_m^{(2)}(k_j r_j) \right], \end{aligned} \quad (\text{C2})$$

$$(T_j)_{13} = (T_j)_{24}^* = i \frac{\pi}{4} \frac{m\beta}{\omega \varepsilon_j} \left( \frac{k_j^2}{k_{j-1}^2} - 1 \right) H_m^{(1)}(k_{j-1} r_j) H_m^{(2)}(k_j r_j), \quad (\text{C3})$$

$$(T_j)_{14} = (T_j)_{23}^* = i \frac{\pi}{4} \frac{m\beta}{\omega \varepsilon_j} \left( \frac{k_j^2}{k_{j-1}^2} - 1 \right) H_m^{(2)}(k_{j-1} r_j) H_m^{(2)}(k_j r_j), \quad (\text{C4})$$

$$(T_j)_{31} = (T_j)_{42}^* = (T_j)_{13} \big|_{\varepsilon \leftrightarrow \mu}, \quad (\text{C5})$$

$$(T_j)_{32} = (T_j)_{41}^* = (T_j)_{14} \big|_{\varepsilon \leftrightarrow \mu}, \quad (\text{C6})$$

$$(T_j)_{33} = (T_j)_{44}^* = (T_j)_{11} \big|_{\varepsilon \leftrightarrow \mu}, \quad (\text{C7})$$

$$(T_j)_{34} = (T_j)_{43}^* = (T_j)_{12} \big|_{\varepsilon \leftrightarrow \mu}. \quad (\text{C8})$$

### References

- [1] D. N. Dinh, S. T. Petcov, N. Sasao, M. Tanaka, and M. Yoshimura, Phys. Lett. B **719**, 154 (2013) [[arXiv:1209.4808](#) [hep-ph]] [[Search INSPIRE](#)].
- [2] M. Yoshimura and N. Sasao, Phys. Rev. D **89**, 053013 (2014) [[arXiv:1310.6472](#) [hep-ph]] [[Search INSPIRE](#)].
- [3] A. Fukumi et al., Prog. Theor. Exp. Phys. **2012**, 04D002 (2012) [[arXiv:1211.4904](#) [hep-ph]] [[Search INSPIRE](#)].
- [4] Y. Miyamoto, et al., Prog. Theor. Exp. Phys. **2014**, 113C01 (2014) [[arXiv:1406.2198](#) [physics.atom-ph]] [[Search INSPIRE](#)].
- [5] Y. Miyamoto, H. Hara, T. Masuda, N. Sasao, M. Tanaka, S. Uetake, A. Yoshimi, K. Yoshimura, and M. Yoshimura, Prog. Theor. Exp. Phys. **2015**, 081C01 (2015) [[arXiv:1505.07663](#) [physics.atom-ph]] [[Search INSPIRE](#)].
- [6] M. Yoshimura, N. Sasao, and M. Tanaka, Phys. Rev. A **86**, 013812 (2012) [[arXiv:1203.5394](#) [quant-ph]] [[Search INSPIRE](#)].

- [7] M. Yoshimura, N. Sasao, and M. Tanaka, Prog. Theor. Exp. Phys. **2015**, 053B06 (2015) [[arXiv:1501.05713](#) [hep-ph]] [[Search INSPIRE](#)].
- [8] E. M. Purcell, Phys. Rev. **69**, 681 (1946).
- [9] D. Kleppner, Phys. Rev. Lett. **47**, 233 (1981).
- [10] P. Goy, J. M. Raimond, M. Gross, and S. Haroche, Phys. Rev. Lett. **50**, 1903 (1983).
- [11] R. G. Hulet, E. S. Hilfer, and D. Kleppner, Phys. Rev. Lett. **55**, 2137 (1985).
- [12] E. Yablonovitch, Phys. Rev. Lett. **58**, 2059 (1987).
- [13] S. John, Phys. Rev. Lett. **58**, 2486 (1987).
- [14] J. D. Joannopoulos, S. G. Johnson, J. N. Winn, and R. D. Meade, *Photonic Crystals*, (Princeton University Press, Princeton, 2008), 2nd ed.
- [15] P. Yeh and A. Yariv, Opt. Commun. **19**, 427 (1976).
- [16] P. Yeh, A. Yariv, and E. Marom, J. Opt. Soc. Am. **68**, 1196 (1978).
- [17] J. D. Jackson, *Classical Electrodynamics*, (John Wiley & Sons, Chichester, 1999), 3rd ed.
- [18] P. Yeh, A. Yariv, and C.-S. Hong, J. Opt. Soc. Am. **67**, 423 (1977).
- [19] Y. Fink, D. J. Ripin, S. Fan, C. Chen, J. D. Joannopoulos, and E. L. Thomas, J. Lightwave Technol. **17**, 2039 (1999).
- [20] J. N. Winn, Y. Fink, S. Fan, and J. D. Joannopoulos, Opt. Lett. **23**, 1573 (1998).
- [21] V. P. Bykov, Sov. Phys. JETP **35**, 269 (1972).
- [22] V. P. Bykov, Sov. J. Quant. Electron. **4**, 861 (1975).
- [23] S. Noda, M. Fujita, and T. Asano, Nat. Photon. **1**, 449 (2007).
- [24] M. Pelton, Nat. Photon. **9**, 427 (2015).
- [25] S. G. Johnson, M. Ibanescu, M. Skorobogatiy, O. Weisberg, T. D. Engeness, M. Soljačić, S. A. Jacobs, J. D. Joannopoulos, and Y. Fink, Opt. Express **9**, 748 (2001).
- [26] M. Ibanescu, S. G. Johnson, M. Soljačić, J. D. Joannopoulos, Y. Fink, O. Weisberg, T. D. Engeness, S. A. Jacobs, and M. Skorobogatiy, Phys. Rev. E **67**, 046608 (2003).
- [27] Y. Xu, R. K. Lee, and A. Yariv, Opt. Lett. **25**, 1756 (2000).